

# Simulating the formation of massive seed black holes in the early Universe. III: The influence of X-rays

Simon C. O. Glover

*Universität Heidelberg, Zentrum für Astronomie, Institut für Theoretische Astrophysik,  
Albert-Ueberle-Straße 2, 69120 Heidelberg, Germany*

7 December 2017

## ABSTRACT

The direct collapse black hole (DCBH) model attempts to explain the observed number density of supermassive black holes in the early Universe by positing that they grew from seed black holes with masses of  $10^4$ – $10^5 M_\odot$  that formed by the quasi-isothermal collapse of gas in metal-free protogalaxies cooled by atomic hydrogen emission. For this model to work,  $H_2$  formation must be suppressed in at least some of these systems by a strong extragalactic radiation field. The predicted number density of DCBH seeds is highly sensitive to the minimum value of the ultraviolet (UV) flux required to suppress  $H_2$  formation,  $J_{\text{crit}}$ . In this paper, we examine how the value of  $J_{\text{crit}}$  varies as we vary the strength of a hypothetical high-redshift X-ray background. We confirm earlier findings that when the X-ray flux  $J_X$  is large, the critical UV flux scales as  $J_{\text{crit}} \propto J_X^{1/2}$ . We also carefully explore possible sources of uncertainty arising from how the X-rays are modelled. We use a reaction-based reduction technique to analyze the chemistry of  $H_2$  in the X-ray illuminated gas and identify a critical subset of 35 chemical reactions that must be included in our chemical model in order to predict  $J_{\text{crit}}$  accurately. We further show that  $J_{\text{crit}}$  is insensitive to the details of how secondary ionization or  $\text{He}^+$  recombination are modelled, but does depend strongly on the assumptions made regarding the column density of the collapsing gas.

**Key words:** astrochemistry – hydrodynamics – methods: numerical – molecular processes – cosmology: theory – quasars: general

## 1 INTRODUCTION

The presence of supermassive black holes (SMBHs) with masses  $\sim 10^9 M_\odot$  and above at redshifts  $z > 6$  (see e.g. Mortlock et al. 2011; Wu et al. 2015; Venemans 2015) is challenging to explain within the context of the standard  $\Lambda$ CDM cosmological model. The problem is one of timescales: if the SMBHs form from seed black holes with masses  $M \sim 10 M_\odot$ , produced as remnants of the earliest generations of massive stars, which then grow by accretion, then there does not seem to be enough time for them to grow to the observed masses by  $z \sim 6$  unless one invokes a length period of super-Eddington accretion (see e.g. the recent review by Johnson & Haardt 2016, and references therein).

Because of this, an alternative model – the direct collapse black hole (DCBH) model – has recently been attracting significant attention. In this model, the seeds of the high redshift SMBHs are not stellar mass black holes, but instead are intermediate mass black holes (IMBHs) with masses of  $10^4$ – $10^5 M_\odot$  that form in some of the earliest protogalaxies. The basic idea is simple. If gas in a protogalaxy with virial temperature  $T_{\text{vir}} > 10^4$  K – an “atomic cooling halo”

– is illuminated by a strong external radiation field, then the formation of molecular hydrogen ( $H_2$ ) within the protogalaxy can be almost completely suppressed (Omukai 2001; Bromm & Loeb 2003). If the gas is also metal-free, i.e. if it has not been enriched by metals from an earlier generation of stars, then the end result is that the gas is unable to cool much below the temperature ( $T \sim 5000$ – $6000$  K) at which Lyman- $\alpha$  and  $H^-$  cooling become ineffective (Omukai 2001; Omukai et al. 2008; Schleicher, Spaans & Glover 2010). It therefore collapses quasi-isothermally, eventually forming a protostar surrounded by a massive accretion disc (Inayoshi, Omukai & Tasker 2014; Becerra et al. 2015; Latif, Schleicher & Hartwig 2016). The high temperature and correspondingly high Jeans mass inhibit fragmentation and also lead to gas accreting onto the newly formed protostar at an extremely high rate,  $\dot{M} \sim 1 M_\odot \text{ yr}^{-1}$ . The outcome of this process is not entirely certain, but the most likely possibilities are either the formation of a supermassive star with  $M \sim 10^5 M_\odot$  that collapses after  $10^5$ – $10^6$  yr to form a massive black hole (Hosokawa et al. 2013), or the formation of a quasi-star, an optically thick massive core whose centre has already collapsed to form a black hole (Begelman, Volon-

teri, & Rees 2006; Begelman 2010; Schleicher et al. 2013). In either case, the end result is an IMBH that subsequently grows into a high-redshift SMBH.

The much larger mass of the seed black hole in the DCBH model greatly alleviates the timing problem referred to above, since considerably less time is required to grow a  $10^4$ – $10^5 M_\odot$  seed to  $\sim 10^9 M_\odot$  than to grow a  $10 M_\odot$  seed to the same final mass. However, one major uncertainty in this model is the strength of the radiation field that is required in order to completely suppress  $\text{H}_2$  formation and prevent fragmentation of the gas. This is often parameterized in terms of  $J_{21}$ , the specific intensity of the radiation field at the Lyman limit in units of  $10^{-21} \text{ erg s}^{-1} \text{ cm}^{-2} \text{ Hz}^{-1} \text{ sr}^{-1}$ , with the minimum value of  $J_{21}$  required for direct collapse being written as  $J_{\text{crit}}$ . The value of  $J_{\text{crit}}$  is important as it strongly influences the likelihood of finding a suitable site for DCBH formation within any given cosmological volume. For instance, Dijkstra et al. (2014) find that varying the value of  $J_{\text{crit}}$  by only a factor of a few changes the predicted number density of DCBH seeds in their model by orders of magnitude. More recently, Inayoshi & Tanaka (2015) have argued that the probability of finding a suitable halo scales as  $J_{\text{crit}}^{-5}$ . Accurate determination of the value of  $J_{\text{crit}}$  is therefore important for assessing the viability of the DCBH model: if the predicted comoving number density of DCBH seeds is too small (i.e. smaller than the observed comoving number density of SMBHs at  $z \sim 6$ ), then the model will be unable to explain the observed high-redshift SMBHs.<sup>1</sup>

Values quoted in the literature for  $J_{\text{crit}}$  span a wide range, from  $\sim 20$  (Inayoshi & Omukai 2011; Glover 2015a) to  $10^5$  (Omukai 2001). There are several reasons for this large scatter. Firstly, the value of  $J_{\text{crit}}$  is known to depend strongly on the spectral shape of the extragalactic radiation field (Shang, Bryan & Haiman 2010; Sugimura, Omukai & Inoue 2014; Latif et al. 2015; Agarwal & Khochfar 2015; Agarwal et al. 2016a,b). In part, this is because this quantity is a relatively crude way of specifying the quantities that actually matter physically, the  $\text{H}^-$  photodetachment rate and the  $\text{H}_2$  photodissociation rate; if we change the shape of the extragalactic radiation field, then generally we will also need to adjust the value of  $J_{21}$  in order to recover the same values for these rates.

Secondly, the value of  $J_{\text{crit}}$  is sensitive to the way in which the effects of  $\text{H}_2$  self-shielding are treated. Typically, this is modeled using a simple shielding function that parameterises the results of more detailed calculations. However, the two functions most commonly used, introduced by Draine & Bertoldi (1996) and Wolcott-Green, Haiman & Bryan (2011), respectively, yield values for  $J_{\text{crit}}$  that can differ by up to an order of magnitude (Sugimura, Omukai & Inoue 2014). In addition, Hartwig et al. (2015) have shown that properly accounting for the velocity structure of the gas in the protogalaxy reduces the effectiveness of self-shielding and decreases  $J_{\text{crit}}$  by roughly a factor of two.

Thirdly, the value of  $J_{\text{crit}}$  that we derive from numerical models of direct collapse can be sensitive to details of the

chemical modelling: the reactions included in the chemical network and the choice of reaction rate coefficients (Glover 2015a,b).

Finally, several studies have shown that  $J_{\text{crit}}$  can also depend on the strength of the X-ray background radiation field illuminating the protogalaxy (Inayoshi & Omukai 2011; Inayoshi & Tanaka 2015; Latif et al. 2015). X-rays penetrate easily into high column density gas and hence are able to increase the fractional ionization of the gas throughout the protogalaxy. The additional free electrons catalyze  $\text{H}_2$  formation via the  $\text{H}^-$  pathway



and hence a larger number of LW photons are required in order to completely suppress  $\text{H}_2$  cooling. We therefore expect that increasing the strength of the X-ray background should increase  $J_{\text{crit}}$ . The studies cited above confirm this expectation, but do not agree when it comes to the strength of the effect.

In this paper we re-examine the impact of X-rays on DCBH formation using a series of simple one-zone models. Building on the work in Glover (2015a), we identify the subset of chemical reactions that it is necessary to include in the chemical network used to model DCBH formation in order to derive reliable results for  $J_{\text{crit}}$ . We also examine how sensitive  $J_{\text{crit}}$  is to the choices made when constructing a model for the effects of X-ray photoionization (e.g. the choice of photoionization cross-sections, the treatment of secondary ionization, or the assumptions regarding shielding), and demonstrate that some of these choices can have a substantial impact on the values of  $J_{\text{crit}}$  we derive when the X-ray background is strong.

The structure of the paper is as follows. In Section 2, we present the numerical method and initial conditions used for our one-zone calculations. We also discuss the reaction-based reduction technique that we use to identify the subset of essential chemical reactions. In Section 3, we explore how  $J_{\text{crit}}$  varies as a function of the X-ray flux  $J_X$  in our fiducial model. In Section 4, we apply our reaction-based reduction technique to the results of our fiducial model and discuss the resulting “reduced” chemical network that this allows us to construct. In Section 5, we examine a number of possible sources of uncertainty in our results, including the treatment of X-ray shielding and the spectral properties of the incident X-ray background. We compare our results with those from previous studies in Section 6 and conclude with a brief summary in Section 7.

## 2 NUMERICAL METHOD

### 2.1 One-zone model

We model the thermal and chemical evolution of the gravitationally-collapsing primordial gas in our simulations using an updated version of the one-zone model presented in Glover (2015a), which itself was derived from a model originally developed by Glover & Savin (2009). Full details of the model are given in these two papers, and so here we simply remind the reader of the basic features and describe

<sup>1</sup> If the predicted number density of DCBH seeds is far too large, then this may also be problematic, but is not immediately fatal for the model, since there is no guarantee that all of the seeds will accrete sufficient gas to become SMBHs by  $z \sim 6$ .

the changes that we have made in order to account for the effects of an X-ray background.

The gas density in the model is assumed to evolve according to

$$\frac{d\rho}{dt} = \frac{\rho}{t_{\text{ff}}}, \quad (3)$$

where  $t_{\text{ff}} = (3\pi/32G\rho)^{1/2}$  is the free-fall time of the gas. The internal energy density  $e$  evolves as

$$\frac{de}{dt} = \frac{p}{\rho^2} \frac{d\rho}{dt} + \Gamma - \Lambda, \quad (4)$$

where  $\Gamma$  and  $\Lambda$  are the radiative heating and cooling rates per unit volume, respectively, and  $p$  is the gas pressure.  $\Gamma$  and  $\Lambda$  are computed using the detailed atomic and molecular cooling function described in Glover & Savin (2009) and updated in Glover (2015a). The only significant change that we have made in the present study is the inclusion of the effects of X-ray heating, which we discuss in the next section.

The chemical evolution of the gas is followed using an updated version of the Glover (2015a) chemical network. The only change that we have made to this network compared to the version presented in Glover (2015a) is the inclusion of eight X-ray induced chemical reactions that were not previously accounted for: the X-ray photoionization of H, D, He, He<sup>+</sup>, Li, H<sub>2</sub> and HD, as well as the double photoionization of He



We describe how we compute the rates of these reactions in Section 2.2 below. Our complete network therefore consists of 30 different primordial chemical species linked by a total of 400 reactions.

We perform simulations with two different models for the spectral shape of the radiation field at energies  $h\nu \leq 13.6$  eV: a  $10^4$  K diluted black-body spectrum (hereafter a T4 spectrum) and a  $10^5$  K diluted black-body spectrum (hereafter a T5 spectrum). Following Haiman, Abel & Rees (2000), we normalize these spectra by specifying their mean specific intensity at the Lyman limit in units of  $10^{-21}$  ergs<sup>-1</sup>cm<sup>-2</sup>Hz<sup>-1</sup>sr<sup>-1</sup>, a quantity that is commonly written as  $J_{21}$ . For both spectra, we assume that there is zero flux at energies above 13.6 eV and below the minimum X-ray energy considered (see Section 2.2.3 below), owing to efficient absorption by atomic hydrogen in the intergalactic medium. Although both of these spectral shapes are highly idealized compared to the spectral energy distributions produced by more realistic models of high redshift galaxies (Sugimura, Omukai & Inoue 2014; Agarwal & Khochfar 2015; Agarwal et al. 2016a,b), they nevertheless are useful for the kind of exploratory study presented in this paper, because they are simple and they allow us to probe the two different physics regimes relevant for the radiative suppression of H<sub>2</sub> cooling in the DCBH scenario. In the case of the T5 spectrum, H<sub>2</sub> photodissociation is the dominant effect and in our fiducial model with this spectrum, H<sub>2</sub> cooling is totally suppressed provided that  $J_{21} \geq J_{\text{crit}} \simeq 1630$  (Glover 2015a), corresponding to an H<sub>2</sub> photodissociation rate in unshielded gas  $k_{\text{dis}} \simeq 2.1 \times 10^{-9}$  s<sup>-1</sup>. With the T4 spectrum, on the other hand, complete suppression of H<sub>2</sub> cooling occurs when  $J_{21} > 18$ , corresponding to an H<sub>2</sub> photodissociation rate of only  $4.9 \times 10^{-11}$  s<sup>-1</sup>. The reason for

this is that in this case, H<sup>-</sup> photo-detachment by lower energy photons, which occurs at a rate  $k_{\text{pd}} = 3.6 \times 10^{-6}$  s<sup>-1</sup>, dramatically reduces the H<sub>2</sub> formation rate, meaning that a much smaller H<sub>2</sub> photodissociation rate is required to reduce the H<sub>2</sub> abundance to the same level. Physically, therefore, changes in the value of  $J_{\text{crit}}$  brought about by X-ray photoionization actually correspond to changes in the values of  $k_{\text{dis}}$  and/or  $k_{\text{pd}}$  that are required in order to completely suppress H<sub>2</sub> cooling.

We account for the effects of H<sub>2</sub> self-shielding using the Wolcott-Green, Haiman & Bryan (2011) shielding function. In order to do so, we need to estimate the H<sub>2</sub> column density. We do this using the same approach as in Glover (2015a,b): we assume that the dominant contribution comes from a constant density core with a radius equal to the Jeans length,  $\lambda_{\text{J}}$ , so that  $N_{\text{H}_2} = n_{\text{H}_2} \lambda_{\text{J}}$ . We do not account for any other sources of opacity, as we expect the continuum opacity of primordial gas to be extremely small at the densities and temperatures relevant for our study (Mayer & Duschl 2005).

## 2.2 Treatment of X-rays

### 2.2.1 X-ray photoionization

The photoionization rate of a species  $m$  due to direct X-ray photoionization can be written in the form

$$R_{\text{d},m} = \int_{\nu_{\text{min}}}^{\nu_{\text{max}}} \frac{4\pi J_{\text{X}}(\nu)}{h\nu} \sigma_m(\nu) e^{-\tau_\nu} d\nu, \quad (6)$$

where  $\nu_{\text{min}}$  and  $\nu_{\text{max}}$  are the minimum and maximum X-ray frequencies considered,  $J_{\text{X}}$  is the mean specific intensity of the X-ray background (discussed in more detail in Section 2.2.3 below),  $\sigma_m(\nu)$  is the photoionization cross-section of species  $m$  at frequency  $\nu$  and  $\tau_\nu$  is the optical depth of the gas at the same frequency. In principle, many different processes contribute towards  $\tau_\nu$ , but in practice, in the conditions relevant for DCBH formation, the dominant contributions come from the photoionization of H and He, so that

$$\tau_\nu = \sigma_{\text{H}}(\nu) N_{\text{H}} + \sigma_{\text{He}}(\nu) N_{\text{He}}, \quad (7)$$

where  $\sigma_{\text{H}}$  and  $\sigma_{\text{He}}$  are the photoionization cross-sections of H and He, and  $N_{\text{H}}$  and  $N_{\text{He}}$  are corresponding column densities. In our fiducial model, we adopt expressions for the photoionization cross-sections taken from Osterbrock (1989) for H and He<sup>+</sup> and Yan, Sadeghpour & Dalgarno (1998, 2001) for He (both single and double photoionization) and H<sub>2</sub>. We assume that the photoionization cross-section of D is the same as that for H, and that the value for HD is the same as that for H<sub>2</sub>. Finally, for Li, we use the cross-section given in Verner et al. (1996).

In Section 5.3, we explore the impact of using the H and He photoionization cross-sections given in Verner et al. (1996) in place of the Osterbrock (1989) and Yan, Sadeghpour & Dalgarno (1998, 2001) values, since the Verner et al. (1996) values have been used in a number of previous studies (e.g. Latif et al. 2015).

To compute  $N_{\text{H}}$  and  $N_{\text{He}}$ , we adopt the same approach as for H<sub>2</sub> above, and set  $N_{\text{H}} = n_{\text{H}} \lambda_{\text{J}}$  and  $N_{\text{He}} = n_{\text{He}} \lambda_{\text{J}}$ , where  $\lambda_{\text{J}}$  is the local value of the Jeans length.

In addition, it is also necessary to account for secondary ionizations caused by the energetic photoelectrons produced

by direct X-ray photoionization. The secondary ionization rate of a species  $m$  can be written as

$$R_{s,m} = \sum_i \frac{n_i}{n_m} R_{d,i} \bar{N}_{\text{ion},m,i} \quad (8)$$

where  $i = \text{H, D, He, He}^+, \text{Li, H}_2$  or HD,  $R_{d,i}$  is the direct photoionization rate of species  $i$ , and  $\bar{N}_{\text{ion},m,i}$  is the number of secondary ionizations of species  $m$  per primary ionization of species  $i$ . To compute  $\bar{N}_{\text{ion},m,i}$ , we first make the simplifying assumption that secondary ionization of any species other than H or He is negligible. This is valid provided that the fractional abundances of  $\text{He}^+$  and  $\text{H}_2$  are much smaller than those of He and H, which is always true for gas in the regime of interest for this study. We then have

$$\bar{N}_{\text{ion},\text{H},i} = R_{d,i}^{-1} \int_{\nu_{\text{min}}}^{\nu_{\text{max}}} \frac{4\pi J_X}{h\nu} \sigma_i e^{-\tau_\nu} N_{\text{ion},\text{H}}(E, x) d\nu, \quad (9)$$

where  $N_{\text{ion},\text{H}}(E, x)$  is the mean number of ionizations produced by an electron with energy  $E = h\nu - h\nu_i$  in gas with fractional ionization  $x$ , and  $h\nu_i$  is the ionization threshold for species  $i$ . Similarly, for helium we have

$$\bar{N}_{\text{ion},\text{He},i} = R_{d,i}^{-1} \int_{\nu_{\text{min}}}^{\nu_{\text{max}}} \frac{4\pi J_X}{h\nu} \sigma_i e^{-\tau_\nu} N_{\text{ion},\text{He}}(E, x) d\nu \quad (10)$$

In our fiducial model, we compute  $N_{\text{ion},\text{H}}(E, x)$  and  $N_{\text{ion},\text{He}}(E, x)$  using the values tabulated by Dalgarno, Yan & Liu (1999) for a mixed gas of H and He. However, in Section 5.4 we examine how much our results change if we instead use the simpler treatment given in Shull & van Steenberg (1985).

### 2.2.2 X-ray heating

The heating rate of the gas due to the photoelectrons produced by X-ray photoionization of a species  $m$  can be written as

$$H_m = \int_{\nu_{\text{min}}}^{\nu_{\text{max}}} \frac{4\pi J_X(\nu)}{h\nu} \sigma_m(\nu) e^{-\tau_\nu} E f_{\text{heat}}(E, x) d\nu, \quad (11)$$

where  $E = h\nu - h\nu_m$  is the energy of the photoelectron and  $f_{\text{heat}}(E, x)$  is the fraction of this energy that is deposited as heat. In our fiducial model, we compute this using the values tabulated by Dalgarno, Yan & Liu (1999) for a mix of H and He, but we also explore the effects of using instead the prescription given in Shull & van Steenberg (1985). Finally, given the heating rate for each species, the total X-ray heating rate per unit volume then follows as

$$\Gamma_X = \sum_m H_m n_m, \quad (12)$$

where  $m = \text{H, D, He, He}^+, \text{Li, H}_2$  or HD. In practice, we find that the dominant contributions generally come from H and He photoionization, since at the densities of interest these species are far more abundant than any of the others.

### 2.2.3 X-ray spectrum

We assume for simplicity that the mean specific intensity of the X-ray background,  $J_X$ , can be represented as a power-law:

$$J_X = J_{X,21} \times 10^{-21} \left( \frac{\nu}{\nu_0} \right)^{-\alpha} \text{ erg s}^{-1} \text{ cm}^{-2} \text{ sr}^{-1} \text{ Hz}^{-1}, \quad (13)$$

where  $h\nu_0 = 1 \text{ keV}$ . In our fiducial model, we set  $\alpha = 1.5$ , following Glover & Brand (2003), but in Section 5.2 we study the effects of varying it between  $\alpha = 1.0$  (as in Kuhlen & Madau 2005 and Jeon et al. 2014) and  $\alpha = 1.8$  (the value adopted by Inayoshi & Tanaka 2015, based on Swartz et al. 2004).

We assume that absorption close to the X-ray sources or in the intergalactic medium attenuates all X-rays below a minimum energy cutoff which by default we take to be  $h\nu_{\text{min}} = 0.5 \text{ keV}$ . In Section 5.2, we explore the effects of varying this default value. In all of our models, we set the maximum photon energy to  $h\nu_{\text{max}} = 30 \text{ keV}$ , but we note that as photons with energies close to  $h\nu_{\text{max}}$  make a negligible contribution to the photoionization and X-ray heating rates, our results are insensitive to this value.

### 2.2.4 Strength of the X-ray background

The strength and spatial variation of the X-ray background at high redshift are poorly constrained. In the local Universe, high mass X-ray binaries dominate the X-ray emission from star-forming galaxies, and so there is a good correlation between the X-ray luminosity and the star formation rate (see e.g. Glover & Brand 2003; Grimm, Gilfanov & Sunyaev 2003; Mineo et al. 2014). If we assume that the same correlation holds for the earliest star-forming galaxies, that these galaxies are forming stars at a roughly constant rate with a standard Salpeter initial mass function, and that the escape fraction of the Lyman-Werner photons produced by these galaxies is close to 100%, then one can show that  $J_{X,21} \sim 4 \times 10^{-6} J_{21}$  (Inayoshi & Tanaka 2015), although this value can change by up to 50% depending upon what one assumes for the shape of the UV and X-ray spectra. For the range of UV field strengths considered in this study, this expression yields values of  $J_{X,21}$  in the range  $10^{-4}$ –0.1. However, it is possible that the number of high mass X-ray binaries per unit of star formation is much higher at high redshift (Fragos et al. 2013a,b), implying that the ratio of  $J_{X,21}$  to  $J_{21}$  could easily be an order of magnitude or more higher. Therefore, in this study we adopt values of  $J_{X,21}$  spanning the range from  $10^{-4}$  to 1.

## 2.3 Initial conditions

As in Glover (2015a), we take the initial gas density to be  $n_0 = 0.3 \text{ cm}^{-3}$ , a value comparable to the mean density of a virialized protogalaxy at  $z = 20$ . In our previous study, we examined several different choices for the initial temperature and chemical composition of the gas, but found that they all yielded very similar results for  $J_{\text{crit}}$ . In this paper, we therefore consider for simplicity only a single set of values. Our choices are the same as those used in runs 2 and 5 in Glover (2015a): an initial temperature  $T_0 = 8000 \text{ K}$ , an initial free electron abundance  $x_{e,0} = 2 \times 10^{-4}$  and an initial  $\text{H}_2$  fractional abundance  $x_{\text{H}_2,0} = 2 \times 10^{-6}$ . For deuterium and lithium, we adopt elemental abundances relative to hydrogen given by  $A_{\text{D}} = 2.6 \times 10^{-5}$  and  $A_{\text{Li}} = 4.3 \times 10^{-10}$ , respectively (Cyburt 2004). We assume that the gas is elec-

**Table 1.** List of simulations

$h\nu_{\min}$ (keV)	$\alpha$	Notes
0.5	1.5	Fiducial model
0.1	1.5	
1.0	1.5	
2.0	1.5	
0.5	1.0	
0.5	1.8	
0.5	1.5	$N_{\text{H}} = n_{\text{H}}\lambda_{\text{J}}/2$
0.5	1.5	Case A $\text{He}^+$ recombination
0.5	1.5	Case B $\text{He}^+$ recombination
0.5	1.5	Secondary ion. from SS85
0.5	1.5	$\sigma_{\text{H}}$ and $\sigma_{\text{He}}$ from V96

SS85 = Shull &amp; van Steenberg (1985)

V96 = Verner et al. (1996)

trically neutral and that the initial  $\text{D}^+$  abundance is a factor of  $A_{\text{D}}$  smaller than the initial  $\text{H}^+$  abundance, so that

$$x_{\text{e},0} = \frac{1}{1 + A_{\text{D}}}x_{\text{H}^+,0} + \frac{A_{\text{D}}}{1 + A_{\text{D}}}x_{\text{D}^+,0}. \quad (14)$$

Lithium and helium are assumed to start in neutral atomic form. We set the starting value of the HD abundance to be  $x_{\text{HD},0} = A_{\text{D}}x_{\text{H}_2,0}$ , and initialize the abundances of all of the other chemical species in our model to zero.

With the initial chemical composition, density and temperature fixed, the remaining free parameters in our one-zone model are those controlling the strength and shape of the optical/UV spectrum ( $J_{21}$ , choice of T4 or T5 spectrum) and the X-ray spectrum ( $J_{\text{X},21}$ ,  $h\nu_{\min}$ ,  $\alpha$ ). In our fiducial setup, we set  $h\nu_{\min} = 1.0$  keV and  $\alpha = 1.5$ , but we also examine additional combinations of these two parameters, as summarized in Table 1. We perform runs with both T4 and T5 spectra, and in each case explore a wide range of different values of  $J_{\text{X},21}$ , ranging from  $10^{-4}$  to 1. For each combination of optical/UV spectrum,  $J_{\text{X},21}$ ,  $h\nu_{\min}$  and  $\alpha$ , we determine  $J_{\text{crit}}$  using the method described in Section 2.4 below.

## 2.4 Determination of $J_{\text{crit}}$

We determine the value of  $J_{\text{crit}}$  in a given model using the same binary search approach as in Glover (2015a). We first select two values of  $J_{21}$ , one very small ( $J_{21,\text{low}}$ ) and the other very large ( $J_{21,\text{high}}$ ), that we can be confident bound the value of  $J_{\text{crit}}$  from below and above. We next calculate a new value of  $J_{21}$  using the equation

$$J_{21,\text{new}} = (J_{21,\text{low}} \times J_{21,\text{high}})^{1/2}. \quad (15)$$

We run a simulation with this new value of  $J_{21}$ , following the collapse of the gas until the H nuclei number density reaches  $n = 10^8 \text{ cm}^{-3}$ . We then examine the outcome of this simulation. If  $\text{H}_2$  cooling is suppressed and the temperature remains  $\sim 6000$  K or higher throughout the collapse of the gas, then we know that  $J_{21,\text{new}} \geq J_{\text{crit}}$ . In this case, we adopt  $J_{21,\text{new}}$  as our new value of  $J_{21,\text{high}}$ . On the other hand, if  $\text{H}_2$  cooling is not suppressed and the gas cools to temperatures  $T \ll 6000$  K during the collapse, then we know that  $J_{21,\text{new}} < J_{\text{crit}}$  and hence adopt it as our new value of  $J_{21,\text{low}}$ . We then calculate a new value of  $J_{21,\text{new}}$  and repeat

the whole procedure. We continue in this fashion until the difference between  $J_{21,\text{low}}$  and  $J_{21,\text{high}}$  is less than 0.2%. At this point we stop, adopting the final value of  $J_{21,\text{new}}$  as our estimate for  $J_{\text{crit}}$ .

## 2.5 Identifying the most important chemical reactions

The detailed model of primordial chemistry that we use in the calculations presented in this paper is too large to use directly in 3D hydrodynamical models of DCBH formation without incurring excessive computational overhead. Therefore, one of the main goals of this paper is to identify an appropriate “reduced” chemical network that includes only those reactions and species that are required for accurately following the time evolution of the  $\text{H}_2$  abundance. In Glover (2015a), we already carried out an analysis of this kind for the case where  $J_{\text{X}} = 0$ . In the present paper, we merely extend this analysis to also consider the case where  $J_{\text{X}} > 0$ . Full details of our approach are given in Glover (2015a), but we summarize the main points here.

We identify important reactions and species using the reaction-based reduction technique developed by Wiebe, Semenov & Henning (2003). Starting from a prescribed set of initial conditions, we first compute the chemical and thermal evolution of the gas for a given value of  $J_{21}$  using our one-zone model. We then select our starting set of important species, which in the present case contains only a single member ( $\text{H}_2$ ). For each species in our set, we compute the production and destruction processes for that species at a series of different output times using the chemical abundances and temperature computed by our one-zone code. We identify “important” processes using the reaction-weighting procedure described in detail in Wiebe, Semenov & Henning (2003) and Glover (2015a). If the set of important reactions includes chemical species that are not in our current set of important species, then we add them to the set and repeat the analysis, proceeding in this fashion until there are no more species or reactions that need to be added.

This reduction procedure generates for each output time a list of the reactions that are required in order to accurately model the  $\text{H}_2$  abundance at that time. The composition of this list may change over time as the density, temperature and chemical abundances change, and so we generate a final list, valid for the whole range of times modelled in our simulations, by combining the individual lists.

The only free parameter in this method enters when we decide whether or not to classify a given reaction as important. We compare the weight for the reaction with a cut-off value  $\epsilon$  and retain only those reactions with weights  $> \epsilon$ . As in Glover (2015a), we conservatively set  $\epsilon = 10^{-4}$ . This yields a set of reactions that allow us to determine  $J_{\text{crit}}$  to within an accuracy of around 1% when compared to the results of models run with the full chemical network.

## 3 THE EFFECT OF X-RAYS ON $J_{\text{CRIT}}$

For our fiducial X-ray model, we explore a range of different values of  $J_{\text{X},21}$ , ranging from  $10^{-4}$  to 1. For each value of  $J_{\text{X},21}$ , we determine the corresponding value of  $J_{\text{crit}}$  using the method described in Section 2.4. Our results are

**Table 2.** Dependence of  $J_{\text{crit}}$  on  $J_{X,21}$  for our fiducial X-ray model

$J_{X,21}$	Spectrum	$J_{\text{crit}}$	$J_{\text{crit}}/J_{\text{crit},0}$
0.0	T4	18.0	1.00
$10^{-4}$	T4	18.5	1.03
$3 \times 10^{-4}$	T4	19.4	1.08
$10^{-3}$	T4	22.2	1.23
$3 \times 10^{-3}$	T4	28.9	1.61
0.01	T4	45.0	2.50
0.03	T4	73.5	4.08
0.1	T4	129	7.17
1.0	T4	357	19.8
<hr/>			
0.0	T5	1630	1.00
$10^{-4}$	T5	1650	1.01
$3 \times 10^{-4}$	T5	1680	1.03
$10^{-3}$	T5	1780	1.09
$3 \times 10^{-3}$	T5	2060	1.26
0.01	T5	2870	1.76
0.03	T5	4610	2.83
0.1	T5	8840	5.42
1.0	T5	34500	21.2

$J_{\text{crit},0}$  is the value of  $J_{\text{crit}}$  when  $J_{X,21} = 0$ .

summarized in Table 2, while in Figure 1 we show how the relative increase in  $J_{\text{crit}}$ , i.e. the value divided by the value in the absence of X-rays,  $J_{\text{crit},0}$ , evolves as we alter  $J_{X,21}$ . We find, in agreement with previous studies, that when  $J_{X,21}$  is small, X-rays have very little influence on  $J_{\text{crit}}$  (Latif et al. 2015; Inayoshi & Tanaka 2015). However, as we increase the X-ray flux, the value of  $J_{\text{crit}}$  steadily increases. The effect is relatively small for  $J_{X,21} < 0.01$ , but at higher values  $J_{\text{crit}} \propto J_{X,21}^{1/2}$ . We also see that the relative increase in  $J_{\text{crit}}$  is very similar for the T4 and T5 spectra, even though the absolute values of  $J_{\text{crit}}$  differ by almost two orders of magnitude.

The relationship between  $J_{X,21}$  and  $J_{\text{crit}}$  that we recover is qualitatively very similar to that found by Inayoshi & Tanaka (2015) using a similar setup.<sup>2</sup> This is no surprise, as the key features are easy to understand physically. Collapsing gas that has reached a density of  $10^4 \text{ cm}^{-3}$  without forming enough  $\text{H}_2$  to cool significantly will remain warm for the rest of the collapse, as above this density collisional dissociation of  $\text{H}_2$  becomes much more effective, while  $\text{H}_2$  cooling becomes substantially less effective (Bromm & Loeb 2003; Inayoshi & Omukai 2011). Therefore, when  $J_{21}$  is close to  $J_{\text{crit}}$ , it is the amount of  $\text{H}_2$  in gas of around this density that determines whether or not the gas can successfully cool. This depends on the formation rate of  $\text{H}_2$ , and since most of the  $\text{H}_2$  forms via the associative detachment reaction



this in turn depends on the formation rate of  $\text{H}^-$ . This ion forms via the radiative association reaction



and so the formation rates of  $\text{H}^-$  and  $\text{H}_2$  both depend directly on the fractional ionization of the gas. When  $J_{X,21}$

<sup>2</sup> We carry out a more quantitative comparison in Section 6 below.

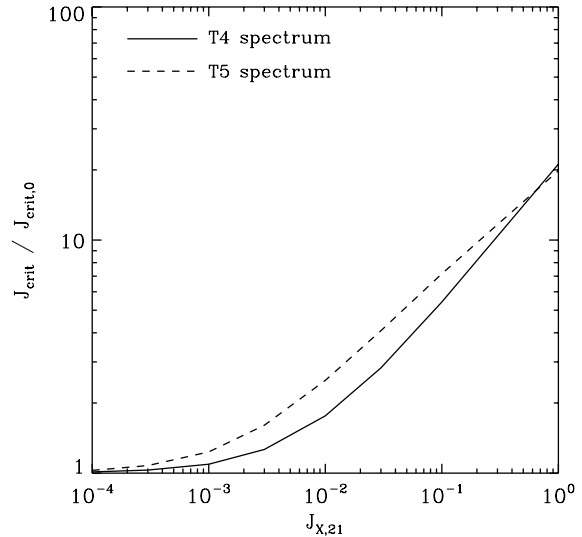


**Figure 1.** Dependence of  $J_{\text{crit}}$  on  $J_{X,21}$ , computed for our fiducial X-ray model for both a T4 spectrum (solid line) and a T5 spectrum (dashed line). In both cases, we normalize the values of  $J_{\text{crit}}$  by the value we obtain in the absence of X-rays,  $J_{\text{crit},0}$ . This value depends strongly on the choice of spectrum: for the T4 spectrum,  $J_{\text{crit},0} = 18.0$ , while for the T5 spectrum,  $J_{\text{crit},0} = 1630$ . However, the growth in  $J_{\text{crit}}/J_{\text{crit},0}$  with increasing  $J_{X,21}$  is very similar in both cases.

is small, X-rays only provide a small amount of additional ionization, and so the  $\text{H}_2$  formation rate is barely affected. When  $J_{X,21}$  is large, on the other hand, X-ray ionization makes a significant contribution to the ionization level of the gas. In the limit where this process dominates, the equilibrium fractional ionization is set primarily by the balance between the X-ray ionization rate  $R_X$  and the radiative recombination rate  $R_{\text{rec}}$ . Since  $R_X \propto J_{X,21}$  and  $R_{\text{rec}} \propto x^2$ , where  $x \equiv n_e/n$  is the fractional ionization of the gas, the result is that  $x \propto J_{X,21}^{1/2}$ . Therefore, in this limit the  $\text{H}_2$  formation rate  $R_{\text{H}_2} \propto J_{X,21}^{1/2}$ , and so the radiation field strength required to suppress  $\text{H}_2$  cooling also scales as  $J_{X,21}^{1/2}$  (see also the similar analysis in Inayoshi & Tanaka 2015).

#### 4 A REDUCED CHEMICAL NETWORK FOR MODELLING THE INFLUENCE OF X-RAYS

Having established how  $J_{\text{crit}}$  varies as a function of  $J_{X,21}$  in our fiducial model, we next analyze the full set of chemical reactions taking place during the evolution of the gas in each run using the reduction technique described in Section 2.5. For each run, we consider  $\sim 18000$  different output times, and use the results of our one-zone model to determine the weight of each reaction at each output time. For each reaction, we then scan through this set of weights and find the maximum value for that reaction. We repeat this procedure for each different value of  $J_{X,21}$  and for runs with  $J_{21}/J_{\text{crit}} = 0.3, 1$  and  $3$ . Finally, we construct our reduced network using only those reactions whose maximum weights exceed  $\epsilon = 10^{-4}$  in at least one run.

The reactions making up our final reduced network are shown in Table 3. The first point to note is that reactions

**Table 3.** List of reactions with maximum reaction weights greater than  $10^{-4}$  in at least one simulation

No.	Reaction
1	$\text{H}_2 + \gamma \rightarrow \text{H} + \text{H}$
2	$\text{H}_2 + \text{H} \rightarrow \text{H} + \text{H} + \text{H}$
3	$\text{H}^- + \text{H} \rightarrow \text{H}_2 + \text{e}^-$
4	$\text{H}_2^+ + \text{H} \rightarrow \text{H}_2 + \text{H}^+$
5	$\text{H}^+ + \text{e}^- \rightarrow \text{H} + \gamma$
6	$\text{H} + \text{e}^- \rightarrow \text{H}^- + \gamma$
7	$\text{H}^- + \gamma \rightarrow \text{H} + \text{e}^-$
8	$\text{H} + \text{H}^+ \rightarrow \text{H}_2^+ + \gamma$
9	$\text{H}_2^+ + \gamma \rightarrow \text{H}^+ + \text{H}$
10	$\text{H} + \text{H} \rightarrow \text{H}^+ + \text{e}^- + \text{H}$
11	$\text{H}^- + \text{H} \rightarrow \text{H} + \text{H} + \text{e}^-$
12	$\text{H} + \text{e}^- \rightarrow \text{H}^+ + \text{e}^- + \text{e}^-$
13	$\text{H}_2^+ + \text{He} \rightarrow \text{HeH}^+ + \text{H}$
14	$\text{H} + \text{He} \rightarrow \text{H}^+ + \text{e}^- + \text{He}$
15	$\text{H}_2 + \text{H}^+ \rightarrow \text{H}_2^+ + \text{H}$
16	$\text{H}_2 + \text{He} \rightarrow \text{H} + \text{H} + \text{He}$
17	$\text{HeH}^+ + \text{H} \rightarrow \text{H}_2^+ + \text{He}$
18	$\text{H} + \text{H} + \text{H} \rightarrow \text{H}_2 + \text{H}$
19	$\text{H}^- + \text{He} \rightarrow \text{H} + \text{He} + \text{e}^-$
20	$\text{H}_2^+ + \text{H} \rightarrow \text{H} + \text{H}^+ + \text{H}$
21	$\text{He} + \text{H}^+ \rightarrow \text{HeH}^+ + \gamma$
22	$\text{H}^- + \text{H}^+ \rightarrow \text{H} + \text{H}$
23	$\text{H}_2^+ + \text{e}^- \rightarrow \text{H} + \text{H}$
24	$\text{HeH}^+ + \text{e}^- \rightarrow \text{He} + \text{H}$
25	$\text{H}^- + \text{H}^+ \rightarrow \text{H}_2^+ + \text{e}^-$
26	$\text{H}^- + \text{e}^- \rightarrow \text{H} + \text{e}^- + \text{e}^-$
<b>27</b>	<b><math>\text{H} + \gamma \rightarrow \text{H}^+ + \text{e}^-</math></b>
<b>28</b>	<b><math>\text{He} + \gamma \rightarrow \text{He}^+ + \text{e}^-</math></b>
<b>29</b>	<b><math>\text{He}^+ + \text{e}^- \rightarrow \text{He} + \gamma</math></b>
<b>30</b>	<b><math>\text{He}^+ + \text{H} \rightarrow \text{He} + \text{H}^+</math></b>
<b>31</b>	<b><math>\text{He}^+ + \text{H}^- \rightarrow \text{He} + \text{H}</math></b>
<b>32</b>	<b><math>\text{He}^+ + \gamma \rightarrow \text{He}^{++} + \text{e}^-</math></b>
<b>33</b>	<b><math>\text{He}^{++} + \text{e}^- \rightarrow \text{He}^+ + \gamma</math></b>
<b>34</b>	<b><math>\text{He}^+ + \text{H} \rightarrow \text{HeH}^+ + \gamma</math></b>
<b>35</b>	<b><math>\text{HeH}^+ + \gamma \rightarrow \text{He} + \text{H}^+</math></b>

Reactions 1–26 are the same as in Glover (2015a). Reactions 27–35 (highlighted in bold) are new in this study.

1–26 are the same as those appearing in the reduced network we obtained in Glover (2015a), where we considered the evolution of the gas in the absence of X-rays. This is unsurprising: the evolution of the gas when  $J_{X,21}$  is very small is essentially the same as in the case  $J_{X,21} = 0$ , and so it is natural that the same chemical reactions will be important in this regime.

The new reactions that need to be added to our reduced reaction network in order to account for the influence of the X-rays, numbers 27–35, are highlighted in bold in the table. We discuss the role that these reactions play in the chemistry below.

### X-ray photoionization of H and He (reactions 27, 28)

The most important effect of the X-rays is of course the additional ionization that they provide to the gas. Although neutral atomic hydrogen (H) is substantially more abundant in the collapsing gas than neutral atomic helium (He), the much larger size of the He photoionization cross-section at X-ray energies means that the rate of direct photoionization

is similar for both species. However, the majority of the ionization is actually secondary ionization resulting from the collision of the energetic photoelectrons with further H and He atoms, and in this case the difference in abundances between H and He results in most of the secondary ionizations being ionizations of H. Ultimately, therefore, most of the free electrons that are produced and that catalyze  $\text{H}_2$  formation come from the ionization of hydrogen. Despite this, it is important to retain helium in the model, since without it we will significantly underestimate the rate of secondary ionization.

### $\text{He}^+$ recombination (reaction 29)

If we include He photoionization, then naturally we must also include  $\text{He}^+$  recombination in order to keep our chemical model consistent. However, its inclusion in our model prompts the question of which rate coefficient we should adopt for this process: should this be the case A rate, the case B rate, or some intermediate treatment? We examine this in detail in Section 5.5 below.

### $\text{He}^+$ charge transfer with H (reaction 30)

When the fractional ionization of the gas is small, this reaction can become competitive with reaction 29 as a sink for  $\text{He}^+$ , despite the fact that the latter has a much larger rate coefficient. The inverse reaction



is unimportant, however, as its high endothermicity means that its rate is strongly suppressed at the temperatures found in the collapsing gas.

### Mutual neutralization of $\text{He}^+$ with $\text{H}^-$ (reaction 31)

The rate coefficient for this reaction is slightly larger than that for the corresponding reaction with  $\text{H}^+$  (reaction 22), and so in some circumstances this can be a non-negligible destruction mechanism for  $\text{H}^-$  despite the fact that in general,  $n_{\text{H}^+} \gg n_{\text{He}^+}$ .

### $\text{He}^+$ photoionization and $\text{He}^{++}$ recombination (reactions 32, 33)

Our reduction algorithm finds that X-ray photoionization of  $\text{He}^+$  to  $\text{He}^{++}$  is marginally important, despite the low abundance of  $\text{He}^+$  relative to He in most of our models. However, we note that taking a slightly larger value of  $\epsilon$  would serve to eliminate this reaction from our reduced network, and so it is possible that our method is being slightly too conservative here. If this reaction is included, then of course it is also necessary to include  $\text{He}^{++}$  recombination, as otherwise the network will not be physically consistent and the  $\text{He}^{++}$  abundance will grow without limit.

### $\text{HeH}^+$ formation from $\text{He}^+$ and H (reaction 34)

We found in our previous analysis that in some circumstances, it was necessary to account for the formation and destruction of the  $\text{HeH}^+$  ion. However, in the conditions studied in that analysis, the  $\text{He}^+$  abundance was always tiny and hence  $\text{HeH}^+$  formation by the radiative association of  $\text{He}^+$  with H was never important, even though the rate coefficient for this reaction is  $\sim 10^4$  times larger than for the corresponding reaction between  $\text{H}^+$  and He (reaction 21). However, once we account for X-ray photoionization,

we recover far larger  $\text{He}^+$  abundances, particularly when  $J_{X,21}$  is large, and hence find that this reaction becomes important.

### $\text{HeH}^+$ photodissociation (reaction 35)

The increased importance of reaction 34 in the presence of X-rays leads to us producing substantially more  $\text{HeH}^+$  than when X-rays are absent. This increases the overall importance of  $\text{HeH}^+$  in the chemical network and therefore means that we need to model its destruction more carefully. As a result, our reduction algorithm finds that when X-rays are present, this reaction becomes a marginally important destruction mechanism for  $\text{HeH}^+$ , even though in the absence of X-rays it falls outside of our reduced set.

## 5 SOURCES OF UNCERTAINTY

In constructing our one-zone model we have made a number of choices that may introduce uncertainties into our estimates for  $J_{\text{crit}}$ . The impact of some of these (e.g. the choice of rate coefficients in cases where the true value is uncertain) has already been explored in Glover (2015b). Here, we examine the effect of uncertainties specifically related to our treatment of X-ray photoionization. Note that our focus is on uncertainties arising from how we construct our numerical model, rather than astrophysical uncertainties such as the value of  $J_{X,21}$  itself.

### 5.1 Shielding length

One important source of uncertainty in one-zone models of the direct collapse process is the treatment of  $\text{H}_2$  self-shielding and X-ray absorption. Commonly, the required column densities of  $\text{H}_2$ , H, He, etc. are obtained in a one-zone model by multiplying the local volume densities of  $\text{H}_2$ , H, He, etc. by a suitably chosen characteristic length scale  $L_c$ . In our fiducial model, we take this to be the Jeans length of the gas at the current density and temperature, i.e.  $L_c = \lambda_J$ ; we note that Latif et al. (2015) make a similar assumption. However, other authors have made different choices for this length scale. For example, Inayoshi & Omukai (2011) and Inayoshi & Tanaka (2015) assume a characteristic scale length of  $L_c = \lambda_J/2$ . More recently, Wolcott-Green, Haiman & Bryan (2016) recommend an even smaller value,  $L_c = \lambda_J/4$ . In reality, all of these choices are at best crude approximations for the behaviour of gas in a real protogalaxy (Wolcott-Green, Haiman & Bryan 2011; Hartwig et al. 2015).

To investigate the impact of our choice of characteristic length scale, we have re-run our models, keeping most parameters the same but setting  $L_c = \lambda_J/2$ . The results of these runs are plotted in Figure 2; we also include the results from our fiducial model, for reference. We see that in the runs with a smaller value of  $L_c$ , the impact of the X-rays is larger. In the runs with a T4 spectrum, decreasing  $L_c$  from  $\lambda_J$  to  $\lambda_J/2$  leads to a 20–30% increase in the value of  $J_{\text{crit}}/J_{\text{crit},0}$  when  $J_{X,21} \geq 0.01$ . In the runs with the T5 spectrum, the effect on  $J_{\text{crit}}/J_{\text{crit},0}$  is significantly larger, between 50% and 75% for the same range of  $J_{X,21}$ . However, if we examine the actual values of  $J_{\text{crit}}$  we obtain in these runs, we find that in the runs with the T4 spectrum, they are only slightly larger than in our fiducial model, while in

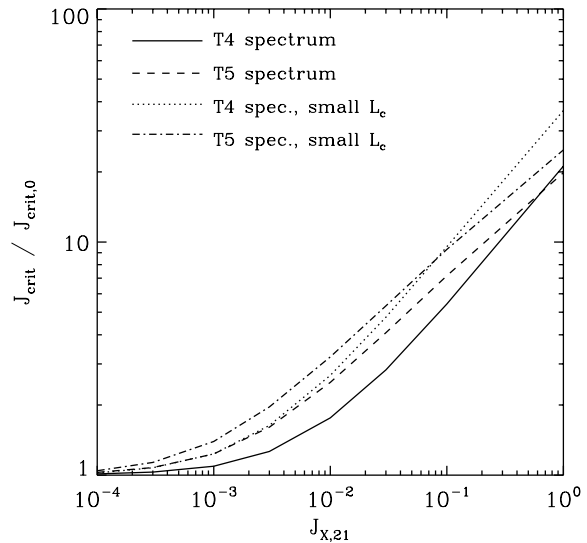


**Figure 2.** Dependence of  $J_{\text{crit}}$  on  $J_{X,21}$  in models where  $L_c = \lambda_J/2$ , computed for a T4 spectrum (dotted line) and a T5 spectrum (dot-dashed line). In both cases, the values of  $J_{\text{crit}}$  are normalized by the value we obtain in the absence of X-rays given the same  $L_c$  and choice of UV-optical spectrum. For comparison, we also show the results from our fiducial model for a T4 spectrum (solid line) and a T5 spectrum (dashed line).

**Table 4.** Dependence of  $J_{\text{crit}}$  on  $J_{X,21}$  in a model where  $L_c = \lambda_J/2$ .

$J_{X,21}$	Spectrum	$J_{\text{crit}}$	$J_{\text{crit}}/J_{\text{crit},0}$
0.0	T4	15.7	1.00
$10^{-4}$	T4	16.4	1.04
$3 \times 10^{-4}$	T4	17.8	1.13
$10^{-3}$	T4	21.9	1.39
$3 \times 10^{-3}$	T4	30.8	1.96
0.01	T4	50.5	3.22
0.03	T4	83.6	5.32
0.1	T4	146	9.30
1.0	T4	390	24.8
0.0	T5	851	1.00
$10^{-4}$	T5	870	1.02
$3 \times 10^{-4}$	T5	915	1.08
$10^{-3}$	T5	1050	1.23
$3 \times 10^{-3}$	T5	1390	1.63
0.01	T5	2280	2.68
0.03	T5	4050	4.76
0.1	T5	8130	9.55
1.0	T5	31200	36.7

$J_{\text{crit},0}$  is the value of  $J_{\text{crit}}$  when  $J_{X,21} = 0$ .

the runs with the T5 spectrum, they are actually smaller (see Table 4). In fact, most of the change in the behaviour of  $J_{\text{crit}}/J_{\text{crit},0}$  is not due to any change in the value of  $J_{\text{crit}}$ ; instead, it is due to a decrease in the value of  $J_{\text{crit},0}$  in the runs with a lower shielding length. This decrease is a result of the fact that in these runs, we now have a smaller column density of  $\text{H}_2$  shielding the collapsing gas, rendering  $\text{H}_2$  self-shielding less effective. When  $J_X$  is small, this effect dominates, and so  $J_{\text{crit}}$  is smaller than in the runs with



larger  $L_c$ . When  $J_X$  is large, on the other hand, the reduced X-ray opacity and consequent increased ionization rate act to offset this effect.

## 5.2 Values of $h\nu_{\min}$ and $\alpha$

The X-ray spectrum adopted in our simulations is specified by three numbers: the mean specific intensity at 1 keV,  $J_{X,21}$ , the spectral slope  $\alpha$ , and the minimum energy cutoff  $h\nu_{\min}$ .<sup>3</sup> We have already examined how  $J_{\text{crit}}$  varies as we change  $J_{X,21}$ . Here, we explore what happens if we vary the other two parameters.

In our fiducial model,  $h\nu_{\min} = 0.5$  keV, but we have also carried out runs with  $h\nu_{\min} = 0.1, 1$  and 2 keV. We find, in agreement with Inayoshi & Tanaka (2015), that our results are insensitive to our choice of  $h\nu_{\min}$  provided that  $h\nu_{\min} \ll 1$  keV. This result is easy to understand. In the density range relevant for determining whether or not the collapsing gas will be able to form enough  $\text{H}_2$  in order to cool, the inferred column density of the protogalaxy ranges from a few times  $10^{22} \text{ cm}^{-2}$  to a few times  $10^{23} \text{ cm}^{-2}$ . This corresponds to an optical depth at 1 keV that ranges from  $\tau \sim 1$  to  $\tau \sim 10$ , or a value at 0.5 keV ranging from  $\tau \sim 10$  to  $\tau \sim 100$ . Therefore, X-ray photons with energies around 1 keV contribute significantly to the photoionization rate of the gas in the critical range of densities, but much softer X-ray photons do not, as they are unable to penetrate deeply enough into the collapsing cloud. Consequently, the value we derive for  $J_{\text{crit}}$  is insensitive to the presence or absence of these very soft X-ray photons, and hence is insensitive to our choice of  $h\nu_{\min}$ , provided that it is less than 1 keV.

If we increase the minimum energy further, to 2 keV, we do find a difference in the behaviour of  $J_{\text{crit}}$ , as illustrated in Figure 3. Increasing  $h\nu_{\min}$  beyond 1 keV has the effect of reducing the X-ray photoionization rate in the dense collapsing gas, since the 1–2 keV soft X-ray photons are responsible for much of the ionization that occurs in our fiducial model. Consequently, we get a smaller fractional ionization for a given  $J_X$ , and recover a smaller value of  $J_{\text{crit}}$ . The impact on  $J_{\text{crit}}$  varies depending on  $J_X$  and our choice of spectrum, but typically, for X-ray backgrounds stronger than  $J_{X,21} \sim 0.01$ , we obtain values of  $J_{\text{crit}}$  that are 30–70% lower than in our fiducial model.

Varying the spectral slope while keeping the minimum X-ray photon energy fixed at  $h\nu_{\min} = 0.5$  keV also has an effect on  $J_{\text{crit}}$ . In Figure 4a, we compare models run with  $\alpha = 1.0, 1.5$  (our fiducial model), and 1.8, with a T4 UV spectrum. In Figure 4b, we show a similar comparison for the case of a T5 spectrum. In both cases, varying  $\alpha$  has a very similar effect. Flattening the X-ray spectrum by decreasing  $\alpha$  leads to a mild increase in  $J_{\text{crit}}$  when  $J_{X,21}$  is large. Conversely, steepening the spectrum by increasing  $\alpha$  causes  $J_{\text{crit}}$  to decrease. The reason for this behaviour is that we normalize our spectra at 1 keV and as we have already seen, X-ray photons below 1 keV do not penetrate deeply enough into the atomic cooling halo in order to significantly affect the chemistry of the gas at the critical period during

<sup>3</sup> Technically, it also depends on the maximum energy cutoff,  $h\nu_{\max}$ , but as previously noted our results are insensitive to this choice provided that it is sufficiently large.

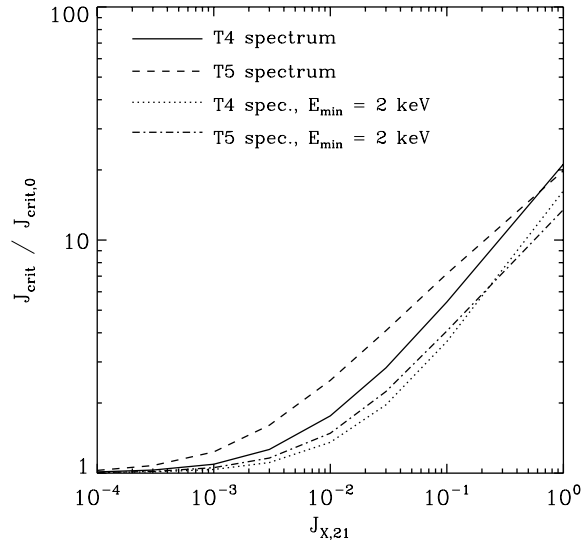


**Figure 3.** Dependence of  $J_{\text{crit}}$  on  $J_{X,21}$  in models where  $h\nu_{\min} = 2$  keV, computed for a T4 spectrum (dotted line) and a T5 spectrum (dot-dashed line). For comparison, we also show the results from our fiducial model for a T4 spectrum (solid line) and a T5 spectrum (dashed line).

its collapse. Therefore, by decreasing  $\alpha$ , we increase the number of X-ray photons at energies high enough to penetrate into and ionize the collapsing gas, and hence increase the ionization rate. Similarly, by increasing  $\alpha$ , we decrease the number of ionizing photons reaching the gas at  $n \sim 10^3 \text{ cm}^{-3}$  and hence decrease the ionization rate.

Figure 3 also demonstrates that the effect that varying  $\alpha$  has on  $J_{\text{crit}}$  is relatively modest. We find the largest impact for  $J_{X,21} \sim 1$  for the T5 spectrum, but even here, changing  $\alpha$  from 1.0 to 1.8 changes  $J_{\text{crit}}$  by no more than 50%. For lower values of  $J_{X,21}$ , or for the T4 spectrum, we find a much smaller effect. We can therefore conclude that the uncertainty in the spectral shape of the X-ray radiation field illuminating the atomic cooling halo introduces at most a 50% uncertainty into our determination of  $J_{\text{crit}}$ . This is not insignificant, but is smaller than the uncertainty introduced by our poor knowledge of the appropriate value of  $J_{X,21}$  at high redshift.

## 5.3 Choice of H and He cross-sections

As mentioned in Section 2.2, in our fiducial model we take values for the H and He photoionization cross-sections from Osterbrock (1989) and Yan, Sadeghpour & Dalgarno (1998, 2001), respectively. However, other authors (e.g. Latif et al. 2015) have used instead the values given in the Verner et al. (1996) compilation of photoionization cross-sections. We have therefore re-run our models using X-ray photoionization and photo-heating rates derived using these alternative cross-sections. We find that in practice, this makes no significant difference to the results of our study. When  $J_X$  is large, we obtain slightly larger values for  $J_{\text{crit}}$  if we use the Verner et al. (1996) cross-sections, but the difference is extremely small,  $\sim 0.2\%$ . When  $J_X$  is small, the difference is likely even smaller, but as our iterative approach only determines  $J_{\text{crit}}$  to within 0.2%, we cannot actually measure

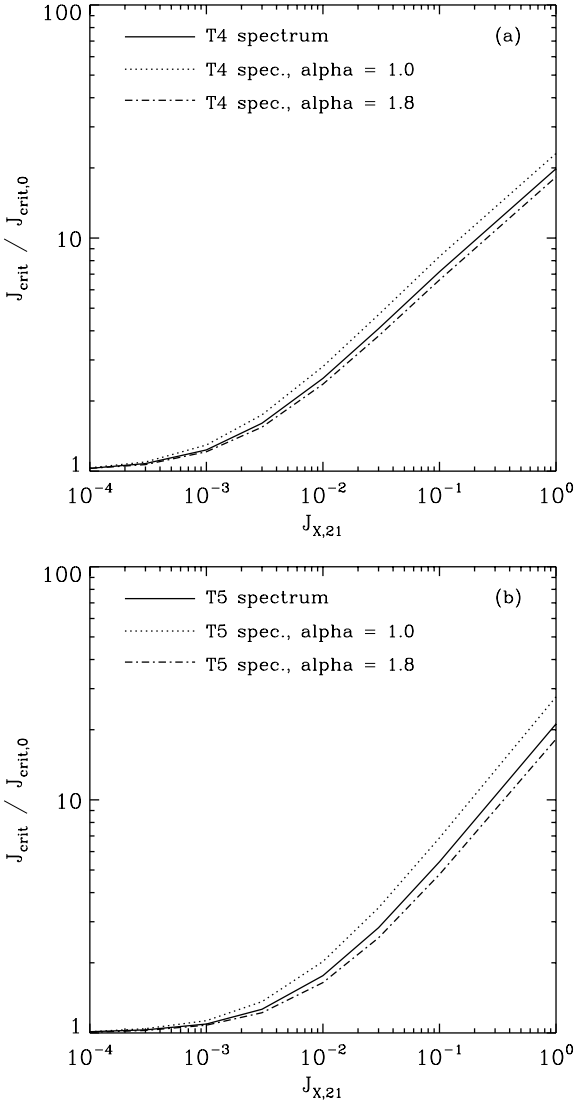


**Figure 4.** (a) Dependence of  $J_{\text{crit}}$  on  $J_{X,21}$  in models in which we vary  $\alpha$ , the slope of the X-ray spectrum. We show results for  $\alpha = 1.0$  (dotted line),  $\alpha = 1.5$  (solid line; our fiducial model), and  $\alpha = 1.8$  (dash-dotted line). All three runs were performed using a T4 ultraviolet spectrum. (b) As (a), but for a T5 ultraviolet spectrum.

it reliably. In both cases, the uncertainty introduced is tiny compared with many of the other uncertainties in the model, and it is therefore safe to neglect it.

The reason that varying the H photoionization cross-section makes so little difference to the outcome becomes clear if we compare the exact expression for  $\sigma_{\text{H}}$  given in Osterbrock (1989) with the analytical fit given in Verner et al. (1996). The two expressions agree extremely well over the whole of the energy range relevant for our study, differing by no more than about 0.2%, and so regardless of which prescription we adopt, we end up with almost exactly the same hydrogen photoionization rate.

The case of helium, however, is a little more interesting. The cross-section for He photoionization given by Yan, Sadeghpour & Dalgarno (1998, 2001) differs from that in Verner et al. (1996) by around 10–20% at the energies of

interest. We might therefore expect the He photoionization rate to differ by a similar amount, but in practice it does not; instead, the difference is only  $\sim 1\%$ . The reason for this is that although reducing the He photoionization cross-section decreases the probability of a given X-ray photon being absorbed by He, it also decreases the optical depth of the gas, for the same reason. Therefore more X-ray photons are able to reach the gas at number densities  $n \sim 10^3\text{--}10^4 \text{ cm}^{-3}$ , the behaviour of which determines whether or not direct collapse occurs. This increased number of photons largely offsets the decreased absorption probability, and the result is that the He photoionization rate barely changes. Consequently, changing the He photoionization cross-section from the Yan, Sadeghpour & Dalgarno (1998, 2001) prescription to the Verner et al. (1996) fit has almost no effect on the ionization state of the gas and hence no effect on the value of  $J_{\text{crit}}$ .

Finally, it is important to note that the fact that our results are insensitive to small changes in  $\sigma_{\text{H}}$  and  $\sigma_{\text{He}}$  does not imply that they are insensitive to large changes in these values. For example, if we use the expression for  $\sigma_{\text{He}}$  given in Osterbrock (1989), which is not intended for use at X-ray energies, then we will dramatically overestimate the He photoionization rate and hence will also overestimate  $J_{\text{crit}}$  (see e.g. the discussion in Latif et al. 2015).

#### 5.4 Secondary ionization model

In our fiducial model, we treat the effects of secondary ionization using values tabulated by Dalgarno, Yan & Liu (1999) for a mix of H and He. However, many studies of the effects of X-rays at high redshift instead use the simple fitting functions given in Shull & van Steenberg (1985), which are based on calculations carried out using older atomic data and which assume that the X-ray photons have energies  $E \gg 100 \text{ eV}$ . We have therefore examined how sensitive our results are to this simplification.

We find that if we use the Shull & van Steenberg (1985) fitting functions in place of the Dalgarno, Yan & Liu (1999) values, we recover values for  $J_{\text{crit}}$  that are between 3–5% higher for X-ray field strengths  $J_{X,21} \geq 0.01$ . The shift towards higher values occurs because the Shull & van Steenberg (1985) fitting functions predict that more of the X-ray energy goes into ionization and less into excitation of H or He, or into heat. However, the difference with the Dalgarno, Yan & Liu (1999) results is small for the photon energies relevant here, and so the impact on  $J_{\text{crit}}$  is also small.

#### 5.5 Treatment of $\text{He}^+$ recombination

Recombination of an  $\text{He}^+$  ion directly into its ground state produces a photon capable of ionizing either hydrogen or helium, while recombination of the same ion into an excited state produces a photon capable of ionizing hydrogen (but not helium) with a probability ranging from 66% at high electron densities ( $n_e \gg 3 \times 10^3 \text{ cm}^{-3}$ ) to 96% at low electron densities ( $n_e \ll 3 \times 10^3 \text{ cm}^{-3}$ ) (Osterbrock 1989). In our fiducial model, we account for these additional ionizing photons as part of our on-the-spot approximation, and also account for the fact that as some of the photons produced by  $\text{He}^+$  recombination into the ground state are absorbed

by hydrogen, not helium, the effective  $\text{He}^+$  recombination rate lies somewhere in between case A and case B. However, it is unclear whether this level of detail is actually necessary in order to accurately determine  $J_{\text{crit}}$ . We have therefore carried out additional runs in which we set the  $\text{He}^+$  recombination rate to either the case A or the case B rate and neglect any H ionizing photons produced by  $\text{He}^+$  recombination. (Note that we adopt the case B rate for  $\text{H}^+$  recombination throughout, as we have already established that  $J_{\text{crit}}$  is highly sensitive to the choice of  $\text{H}^+$  recombination rate coefficient – see Glover 2015b).

We find that in practice, our results do not depend on how we treat  $\text{He}^+$  recombination. We obtain extremely similar values for  $J_{\text{crit}}$  regardless of whether we adopt the case A rate, the case B rate, or the more accurate treatment described above. To help us understand why this is the case, we have examined the rates of the reactions responsible for forming and destroying  $\text{He}^+$  in the density range relevant for determining  $J_{\text{crit}}$ ,  $n \sim 10^3\text{--}10^4 \text{ cm}^{-3}$ . We find that because of the low fractional ionization at these densities,  $\text{He}^+$  recombination is not the main process responsible for removing  $\text{He}^+$  ions from the gas. Instead, the removal of  $\text{He}^+$  is dominated by charge transfer with atomic hydrogen,



Consequently, even fairly large changes in the  $\text{He}^+$  recombination rate have only a very small influence on the  $\text{He}^+$  abundance, and hence on the contribution that  $\text{He}^+$  makes towards the total fractional ionization. As a result of this, changing the  $\text{He}^+$  recombination rate has almost no influence on the  $\text{H}_2$  formation rate, and hence almost no influence on  $J_{\text{crit}}$ .

## 6 COMPARISON WITH PREVIOUS STUDIES

The influence of X-rays on the value of  $J_{\text{crit}}$  has previously been investigated in studies by Inayoshi & Omukai (2011), Latif et al. (2015) and Inayoshi & Tanaka (2015). However, as noted by Latif et al. (2015), in their original study Inayoshi & Omukai (2011) adopted the approximate helium photoionization cross-section given in Osterbrock (1989), which is 1–2 orders of magnitude too large for photon energies of a few keV. Therefore, although their paper is important as it was the first one to point out the potential importance of X-ray ionization for the direct collapse black hole scenario, their numerical results for the dependence of  $J_{\text{crit}}$  on  $J_X$  are incorrect. For this reason, we do not compare our results with their study, but instead restrict our attention to the more recent studies by Latif et al. (2015) and Inayoshi & Tanaka (2015).

Latif et al. (2015) examine the effects of hard X-rays, with a minimum energy of 2 keV, within their 3D simulations of direct collapse black hole formation. They find that even large X-ray fluxes have a relatively small impact on  $J_{\text{crit}}$ , increasing it by roughly a factor of 2 for  $J_{X,21} = 0.1$  and a factor of 4 for  $J_{X,21} = 1$ . For comparison, in our fiducial model,  $J_{\text{crit}}/J_{\text{crit},0} \sim 5$  and  $\sim 20$  for the same two values of the X-ray background field strength. Some of the difference between the two models is due to the fact that they ignore X-ray photons at energies below 2 keV, since these actually dominate the photoionization at the relevant densities.

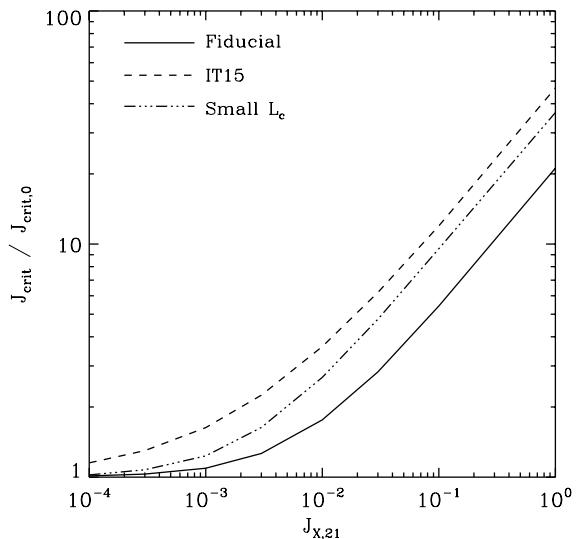


**Figure 5.**  $J_{\text{crit}}$  as a function of  $J_{X,21}$ , plotted for our fiducial T5 model (solid line), the Inayoshi & Tanaka (2015) model with a T5 spectrum (dashed line) and a modification of our model in which we set the shielding length to  $L_c = \lambda_J/2$  to better match the procedure used in Inayoshi & Tanaka’s study. Note that the difference between Inayoshi & Tanaka’s results at very small  $J_X$  and our own is due to the fact that their fitting function does not accurately represent their results for  $J_{X,21} \sim 10^{-4}$ : in their one-zone models, they find that  $J_{\text{crit}}/J_{\text{crit},0} = 1$  here, in good agreement with our results.

However, this does not completely explain the difference: if we compare our results from runs with  $h\nu_{\text{min}} = 2 \text{ keV}$  (see Section 5.2) with their results, we see that our one-zone model still predicts roughly a factor of two larger impact on  $J_{\text{crit}}$  than they find in their 3D runs. It is unclear why this difference exists, but it is possible that it reflects a systematic difference between the effectiveness of X-rays in one-zone models compared to 3D models. In this context, it is interesting to note that Inayoshi & Tanaka (2015) also examine the case where  $h\nu_{\text{min}} = 2 \text{ keV}$  and recover values for  $J_{\text{crit}}/J_{\text{crit},0}$  at  $J_{X,21} = 0.1$  and 1 that agree well with our results and disagree with the Latif et al. (2015) results. Ultimately, additional 3D simulations of DCBH formation in the presence of X-rays will likely be needed in order to understand the cause of this discrepancy.

Turning to the study by Inayoshi & Tanaka (2015), we begin by noting that they do not consider the case of a T4 spectrum, so we cannot compare our results with theirs for that case. However, they do carry out runs with a T5 spectrum (and also spectra with  $T_{\text{eff}} = 2 \times 10^4$  and  $3 \times 10^4 \text{ K}$ ). In Figure 5, we compare the results from our fiducial T5 model (solid line) to the values predicted by the fitting function given by Inayoshi & Tanaka (2015) for the T5 case.<sup>4</sup> We see that Inayoshi & Tanaka (2015) find values of  $J_{\text{crit}}/J_{\text{crit},0}$  that are roughly a factor of two larger than ours when  $J_X$  is large. There is also a small discrepancy when  $J_X$  is very small, but this simply reflects the fact that their fitting function overestimates  $J_{\text{crit}}$  slightly when  $J_{X,21} \ll 10^{-3}$  compared to their

<sup>4</sup> This function is  $J_{\text{crit}}/J_{\text{crit},0} = (1 + J_{X,21}/0.0021)^{0.62}$ .

one-zone results (see e.g. Figure 1 in Inayoshi & Tanaka 2015).

Much of the difference between the results from Inayoshi & Tanaka (2015) at large  $J_X$  and those from our fiducial model is due to the different assumptions we make regarding the shielding length. In our fiducial model, we assume that  $L_c = \lambda_J$ , whereas in their model, Inayoshi & Tanaka (2015) assume that  $L_c = \lambda_J/2$ . As we have already seen in Section 5.1, this difference has a significant effect on the value of  $J_{\text{crit}}$ . If we compare their results with those from a run in which we also set  $L_c = \lambda_J/2$  (the dot-dashed line in Figure 5), we find much better agreement, with a maximum difference of around 20% when  $J_{X,21} = 1$ . This remaining difference is likely due to differences in the chemical model used in the different simulations: as we have already seen in Glover (2015a,b), differences in network design and the choice of chemical rate coefficients can easily introduce uncertainties of this size or larger into  $J_{\text{crit}}$ .

## 7 SUMMARY

In this paper, we have examined the impact of a soft X-ray background on the strength of the UV radiation field required in order to suppress  $\text{H}_2$  formation in an atomic cooling halo, thereby allowing for direct collapse black hole formation to occur. We confirm the earlier results of Inayoshi & Tanaka (2015) that the X-rays have a significant effect on the value of  $J_{\text{crit}}$  for X-ray field strengths  $J_{X,21} > 0.01$  and that in the limit of large  $J_{X,21}$ , the critical UV field strength scales as  $J_{\text{crit}} \propto J_{X,21}^{1/2}$ . However, we recover values of  $J_{\text{crit}}/J_{\text{crit},0}$  (the value in the absence of an X-ray background) that are up to a factor of two smaller than those reported by Inayoshi & Tanaka (2015). This difference is largely due to the different assumptions we make regarding the amount of shielding against X-ray photoionization provided by the gas within the atomic cooling halo: we adopt a shielding length  $L_c = \lambda_J$ , whereas Inayoshi & Tanaka (2015) adopt a value a factor of two smaller,  $L_c = \lambda_J/2$ . This sensitivity to the adopted shielding prescription emphasizes the need for the effect of X-rays to be re-examined in 3D studies that can accurately account for the true 3D gas distribution, but this lies outside of the scope of the present study.

We have also used the reaction-based reduction technique developed by Wiebe, Semenov & Henning (2003) and first applied to DCBH formation by Glover (2015a) to identify the minimum subset of reactions needed to accurately determine  $J_{\text{crit}}$  from simulations of the kind carried out here. This minimum subset consists of all 26 of the reactions in the reduced network of Glover (2015a), plus an additional 9 reactions that are required when  $J_X \gg 0$ .

Finally, we have carefully examined a number of possible sources of uncertainty in the modelling of the X-ray background and its effect on the collapsing gas. We show that the results we recover for  $J_{\text{crit}}$  are independent of our choice of parameterization for the H and He photoionization cross-sections, provided we choose fits that are appropriate for use at X-ray energies. Our results are also independent of the accuracy of our treatment of  $\text{He}^+$  recombination, as in practice, charge transfer with atomic hydrogen is a more important loss route for  $\text{He}^+$  in the physical conditions of interest. We also demonstrate that  $J_{\text{crit}}$  is only very weakly

dependent on the prescription used to treat secondary ionization.

On the other hand, we demonstrate that our results are quite sensitive to the way in which shielding by neutral hydrogen and helium elsewhere in the halo is accounted for, as already noted above. In addition, the values of  $J_{\text{crit}}$  we recover depend on the slope assumed for the X-ray background, although varying the spectral index from  $\alpha = 1$  to  $\alpha = 1.8$  alters  $J_{\text{crit}}$  by at most 50% in the limit of large  $J_X$ . Finally, our results are independent of the low energy cutoff chosen for the X-ray spectrum,  $h\nu_{\text{min}}$ , provided this is less than 1 keV. However, increasing it above 1 keV leads to a substantial decrease in the values we obtain for  $J_{\text{crit}}$  when  $J_X$  is large.

## ACKNOWLEDGEMENTS

The author would like to thank B. Agarwal, J. Wolcott-Green, K. Inayoshi and J. Mackey for useful discussions on the topics of X-ray photoionization and DCBH formation. Financial support for this work was provided by the Deutsche Forschungsgemeinschaft via SFB 881, “The Milky Way System” (sub-projects B1, B2 and B8) and SPP 1573, “Physics of the Interstellar Medium” (grant number GL 668/2-1), and by the European Research Council under the European Community’s Seventh Framework Programme (FP7/2007-2013) via the ERC Advanced Grant STARLIGHT (project number 339177).

## REFERENCES

- Agarwal, B., & Khochfar, S. 2015, MNRAS, 446, 160  
 Agarwal, B., Smith, B., Glover, S., Natarajan, P., & Khochfar, S. 2016a, MNRAS, 459, 4209  
 Agarwal, B., Cullen, F., Khochfar, S., Klessen, R., Glover, S., & Johnson, J. 2016b, MNRAS, submitted  
 Becerra, F., Greif, T. H., Springel, V., & Hernquist, L. E. 2015, MNRAS, 446, 2380  
 Begelman, M. C., Volonteri, M., & Rees, M. J. 2006, MNRAS, 370, 289  
 Begelman, M. C. 2010, MNRAS, 402, 673  
 Bromm, V., & Loeb, A. 2003, ApJ, 596, 34  
 Cyburt, R. H. 2004, Phys. Rev. D, 70, 023505  
 Dalgarno, A., Yan, M., & Liu, W. 1999, ApJS, 125, 237  
 Dijkstra, M., Ferrara, A., & Mesinger, A. 2014, MNRAS, 442, 2036  
 Draine, B. T., & Bertoldi, F. 1996, ApJ, 468, 269  
 Fragos, T., et al., 2013a, ApJ, 764, 41  
 Fragos, T., Lehmer, B. D., Naoz, S., Zezas, A., & Basu-Zych, A. 2013b, ApJ, 776, L31  
 Glover, S. C. O., & Brand, P. W. J. L. 2003, MNRAS, 340, 210  
 Glover, S. C. O., & Savin, D. W. 2009, MNRAS, 393, 911  
 Glover, S. C. O. 2015a, MNRAS, 451, 2082  
 Glover, S. C. O. 2015b, MNRAS, 453, 2901  
 Grassi, T., Bovino, S., Schleicher, D. R. G., Prieto, J., Seifried, D., Simoncini, E., & Gianturco, F. A. 2014, MNRAS, 439, 2386  
 Grimm, H.-J., Gilfanov, M., & Sunyaev, R. 2003, MNRAS, 339, 793

- Haiman, Z., Abel, T., & Rees, M. J. 2000, *ApJ*, 534, 11
- Hartwig, T., Glover, S. C. O., Klessen, R. S., Latif, M. A., & Volonteri, M. 2015, *MNRAS*, 452, 1233
- Hosokawa, T., Yorke, H. W., Inayoshi, K., Omukai, K., & Yoshida, N. 2013, *ApJ*, 778, 178
- Inayoshi, K., & Omukai, K. 2011, *MNRAS*, 416, 2748
- Inayoshi, K., Omukai, K., & Tasker, E. 2014, *MNRAS*, 445, L109
- Inayoshi, K., & Tanaka, T. L. 2015, *MNRAS*, 450, 4350
- Jeon, M., Pawlik, A. H., Bromm, V., Milosavljević, M. 2014, *MNRAS*, 440, 3778
- Johnson, J. L., & Haardt, F. 2016, *PASA*, 33, 7
- Kuhlen, M., & Madau, P. 2005, *MNRAS*, 363, 1069
- Latif, M. A., Bovino, S., Grassi, T., Schleicher, D. R. G., & Spaans, M. 2015, *MNRAS*, 446, 3163
- Latif, M. A., Schleicher, D. R. G., & Hartwig, T. 2016, *MNRAS*, 458, 233
- Mayer, M., Duschl, W. J. 2005, *MNRAS*, 358, 614
- Mineo, S., Gilfanov, M., Lehmer, B. D., Morrison, G. E., & Sunyaev, R. 2014, *MNRAS*, 437, 1698
- Mortlock, D. J., et al. 2011, *Nature*, 474, 616
- Omukai, K., 2001, *ApJ*, 546, 635
- Omukai, K., Schneider, R., & Haiman, Z. 2008, *ApJ*, 686, 801
- Osterbrock, D. E. 1989, *Astrophysics of gaseous nebulae and active galactic nuclei*, (Mill Valley: University Science Books)
- Schleicher, D. R. G., Spaans, M., & Glover, S. C. O. 2010, *ApJ*, 712, L69
- Schleicher, D. R. G., Palla, F., Galli, D., & Latif, M. 2013, *A&A*, 558, A59
- Shang, C., Bryan, G. L., & Haiman, Z. 2010, *MNRAS*, 402, 1249
- Shull, J. M., & van Steenberg, M. E. 1985, *ApJ*, 298, 268
- Sugimura, K., Omukai, K., & Inoue, A. K. 2014, *MNRAS*, 445, 544
- Swartz, D. A., Ghosh, K. K., Tennant, A. F., & Wu, K., 2004, *ApJS*, 154, 519
- Venemans, B. P. et al. 2015, *ApJ*, 801, L11
- Verner, D. A., Ferland, G. J., Korista, K. T., & Yakovlev, D. G. 1996, *ApJ*, 465, 487
- Wiebe, D., Semenov, D., & Henning, Th. 2003, *A&A*, 399, 197
- Wolcott-Green, J., Haiman, Z., & Bryan, G. L. 2011, *MNRAS*, 418, 838
- Wolcott-Green, J., Haiman, Z., & Bryan, G. L. 2016, *MNRAS*, submitted; arXiv:1609.02142
- Wu, X.-B., et al. 2015, *Nature*, 518, 7540
- Yan, M., Sadeghpour, H. R., & Dalgarno, A. 1998, *ApJ*, 496, 1044
- Yan, M., Sadeghpour, H. R., & Dalgarno, A. 2001, *ApJ*, 559, 1194